

## NUMERICAL ANALYSIS OF PLASMONIC NANO HOLE DIAMETERS IN THIN GOLD FILMS

---

**Verónica Iraís Solís-Tinoco<sup>1,3\*</sup>, Ana Elisa Pérez Tovar<sup>2</sup>,  
Hatzyri Ismerai Hernandez Mercado<sup>2</sup>,  
Berenice Montiel Pitalua<sup>2</sup>, Karen Lyzeth Alonzo García<sup>2</sup>,  
Luis Alfonso Villa-Vargas<sup>1</sup>, Marco Antonio Ramírez-Salinas<sup>1</sup>,  
Miguel Ángel Alemán-Arce<sup>1</sup>**

<sup>1</sup>Centro de Investigación en Computación del Instituto Politécnico Nacional, Laboratorio de Microtecnología y Sistemas Embebidos. Ciudad de México, 07738, México.

<sup>2</sup>Unidad Profesional Interdisciplinaria en Ingeniería y Tecnologías Avanzadas UPIITA-IPN. Ingeniería Biónica. Ciudad de México, C.P. 07340, México.

<sup>3</sup>Instituto de Ciencias Aplicadas y Tecnología, Universidad Nacional Autónoma de México, Ciudad de México, 04510, México.

\*irais.solis@cic.ipn.mx

## Abstract

We present a numerical analysis of the optical properties of a gold nanohole with diameters ranging from 90 nm to 130 nm to examine the behavior of the LSPR phenomenon. We utilized COMSOL Multiphysics software to calculate the changes in optical transmittance, absorbance, and reflectance over a wavelength range from 400 nm to 900 nm. The calculated transmittance curves for diameters of 90 nm, 100 nm, 110 nm, 120 nm and 130 nm show that the LSPR initial position shifts from 675 nm to 690 nm. A similar behaviour was observed in the absorbance and reflectance spectra. The maximum absorbance ranges from 686 nm to 710 nm while the reflectance maximum shifts from 659 nm to 673 nm. The results suggest that these diameters are suitable for generating the LSPR phenomenon; however, the 100 nm diameter showed the highest electromagnetic field value of  $9.28 \times 10^8$  V/m. Additionally, an optical transducer based on gold nanoholes with a diameter of 100 nm is feasible to fabricate using low-cost techniques like colloidal lithography. Therefore, this work provides a tool for students and researchers to design optical transducers based on nanostructures, leveraging the potential offered by numeric simulations.

**Keywords:** numerical simulation, gold nanohole, plasmonics, diameters.

## 1. Introduction

The fascination with the optical properties of metal nanostructures arises from their distinctive phenomenon called localized surface plasmon resonance (LSPR). This phenomenon is caused by collective oscillations of electron gas on the surface of metal nanostructures, particularly noble metals like gold and silver. These oscillations take place within a surrounding dielectric medium. LSPR is characterized by distinct spectral peaks in optical absorption, transmittance, and reflectance, as well as strong enhancements in the electromagnetic field, which occur at specific wavelengths [1, 2]. The position of these peaks is highly sensitive to changes in the refractive index of the surrounding dielectric medium. Therefore, any molecules adsorbed at the nanoparticle surface induce a modification of the local refractive index consequently causing a shift of the LSPR position [3], which forms the basis for detecting analytes using LSPR sensors [4 - 6].

Researchers have proposed that LSPR sensing techniques utilizing nanoparticle or nanostructures substrates could retain the advantages of traditional SPR methods while significantly expanding their scientific and technological applicability. This is because LSPR sensing fundamentally relies on straightforward optical extinction measurements, exhibits minimal temperature sensitivity, and can be implemented using widely available, standard laboratory equipment. Thereby, nanoparticle based LSPR sensing could open challenging application avenues across diverse fields [7, 8]. For example, LSPR sensors have been applied to detect bladder cancer [9]; determining chemicals in urine such as creatinine, albumin and glucose, three of the most abundant components in urine [10]; and detecting cardiovascular disease [11]; among many others.

LSPR sensor sensitivity can be influenced by nanostructure size, shape, aspect ratio, spacing, and material dielectric constant. In this way, optimizing the nanostructure geometry is critical to maximize sensitivity and the limit of detection (LOD) and take full advantage of the material's properties. For instance, while spherical gold nanostructures have advantages in terms of chemistry and fabrication, other shapes such as stars, pyramids, tips, and rods may be more sensitive to changes in the refractive index [12 - 21]. Among the nanostructures, metallic nanoholes are very attractive due to their extraordinary optical transmission that produces LSPR. Hence, nanoholes have been

employed in diverse application areas such as sensing. Those have been used for the direct optical probing of proteins, viruses, bacteria, and even cancer cells [22 - 25].

Consequently, the research and fabrication of noble metal nanostructures as optical transducers have gained importance for the development of LSPR sensor technology, therefore, we can discover a multitude of techniques for their creation [26 -29]. However, selecting each transducer parameter based on nanoholes is challenging, and an error could result in significant time and material losses.

Numerical simulations have emerged as a potent tool for researching and designing plasmonic transducers allowing the study of optical parameters in a virtual environment, reducing the need to manufacture them. Also, they facilitate testing a multitude of design parameters for optical transducers, including geometry, dimensions, materials, light excitation sources, and dielectric mediums. This enables the evaluation of their impact on the transducer's optical properties, facilitating informed decision-making for future manufacturing projects.

The ability to use the software and all its functionalities may require time for users to learn because of the extended list of attributes involved in numerical simulations and its properties. Also, obtaining useful information to guide the step-by-step design of an optical transducer in such detailed way is a challenging task. In this work, we describe the design of a plasmonic transducer based on gold nanoholes. A single gold nanohole is simulated using COMSOL Multiphysics 6.1, exploring different diameters ranging from 90 nm to 130 nm within a 300 nm by 300 nm area on a glass substrate.

The nanohole is excited by a white light source reaching wavelengths from 400 nm to 900 nm, with air as the dielectric medium. We start by performing a numerical analysis to evaluate the impact of nanohole diameter on significant optical properties such as transmittance, reflectance and absorbance, and determine the wavelength of the LSPR, as well as the distribution of the electromagnetic field. The objective of this numerical analysis is to illustrate how variations in nanohole size affect optical properties, including the position of the LSPR and the distribution of the electric field, understanding these factors is determining for designing effective plasmonic transducers and developing advanced optical sensors.

## 2. Methodology

This section outlines the methodology employed to design and execute a simulation aimed at analyzing the behavior and response of a plasmonic nanohole with different diameters. The structural configuration consists of a glass substrate supporting a 20 nm gold film with a singular nanohole, and air serving as the dielectric medium. The system is stimulated by an electromagnetic field with a wavelength ranging from 400 nm to 900 nm. This simulation’s main objective is to investigate the impact of nanohole diameter on its optical properties. To achieve this, the diameters at values of 90 nm, 100 nm, 110 nm, 120 nm, and 130 nm were varied.

To generate this simulation, COMSOL Multiphysics software 6.1, which enables the customization of simulation parameters, including physics modules, system geometry, boundaries, materials, and other physical parameters, was used. Additionally, with this software, graphical representations of three optical properties, absorbance, transmittance, and reflectance over the wavelength range were obtained. Furthermore, COMSOL enables to visualize the electric field behavior around the gold nanohole. These graphs and animation provide valuable information about the nanohole’s optical behavior. This section details each phase of the methodology to generate this 3D simulation, including simulation set-up, parameter variation, and analysis techniques. This is shown in Figure 1.

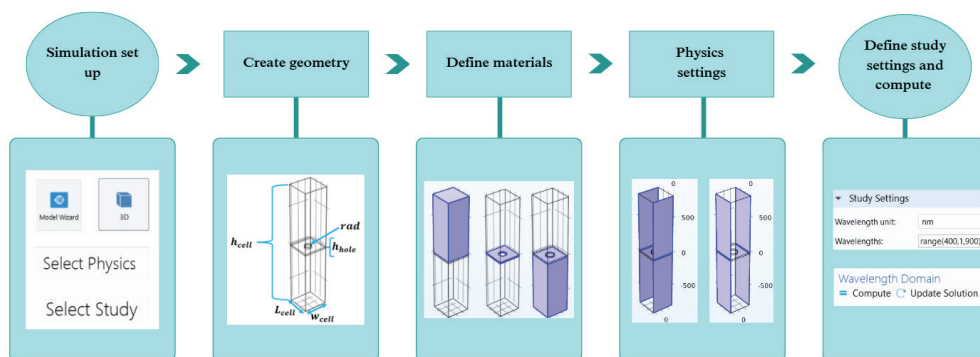


Figure 1. Phases of the methodology to generate the 3D simulation for the analysis of the behavior and response of a nanohole with different diameters, including simulation set-up, parameter variation and analysis techniques.

## 2.1. COMSOL Simulation Settings

First, the simulation in COMSOL Multiphysics was set up, as summarized in Table 1. The first step was to create a new model with Model Wizard, and then the modeling space was established as three-dimensional (3D). Next, the electromagnetic waves, Frequency domain (ewfd) interface was selected in the Physics window, allowing the simulation of the electromagnetic source across a range of frequencies and its interaction with the plasmonic nanohole structure. Finally, on the Study selection page, the wavelength domain was chosen to compute the structure's optical properties versus wavelength and the propagation of electromagnetic waves through it.

Settings	Details
Space dimension	3D
Physics	Electromagnetic waves, Frequency domain (ewfd)
Study	Wavelength domain

Table 1. COMSOL simulation settings for the gold nanohole.

## 2.2. Nanohole geometry

Figure 2a illustrates the cell design and the parameters required to design the gold nanohole in COMSOL Multiphysics. To start building the nanohole geometry, the width, length and height of each structure (glass, gold and air) were defined: **w<sub>cell</sub>** for the cell width, **L<sub>cell</sub>** for the cell length, **h<sub>cell</sub>** for the cell height, **h<sub>hole</sub>** for the height of the gold nanofilm, and **rad** for the nanohole radius, as shown in Figure 2b.

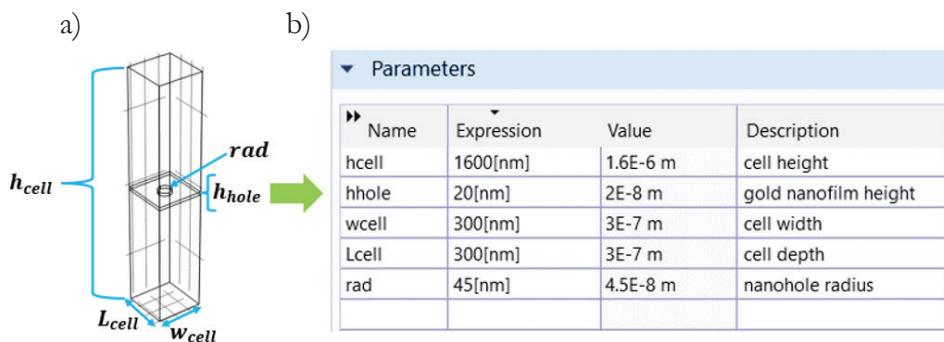


Figure 2. Parameters to design the gold nanohole. (a) Represents the nanohole geometry and the parameters of each section. (b) Parameters used to design nanohole geometry.

COMSOL Multiphysics offers predetermined primitive structures. To create the cell, the block option from the top menu twice was selected, resulting in two blocks: one for the whole structure, designated as block1, as shown in Figure 3a, and the second one for the thin 20 nm gold film, designated as block 2, illustrated in Figure 3b. Then, we select the cylinder option to create the nanohole inside the gold film, as shown in Figure 3c. The following Table 2 summarizes the parameters (width, length, height, base) to configure each structure. While all the measures remain constant, the diameter value ranges from 90 to 130 nm.

Size and shape	Block 1	Block 2	Cylinder	
<b>Width</b>	W <sub>cell</sub>	w <sub>cell</sub>	Radius	rad
<b>Depth</b>	L <sub>cell</sub>	L <sub>cell</sub>	Height	h <sub>hole</sub>
<b>Height</b>	H <sub>cell</sub>	h <sub>hole</sub>	Position	Z -10
<b>Base</b>	Center	Center		

Table 2. Parameters to create each section of nanohole geometry.

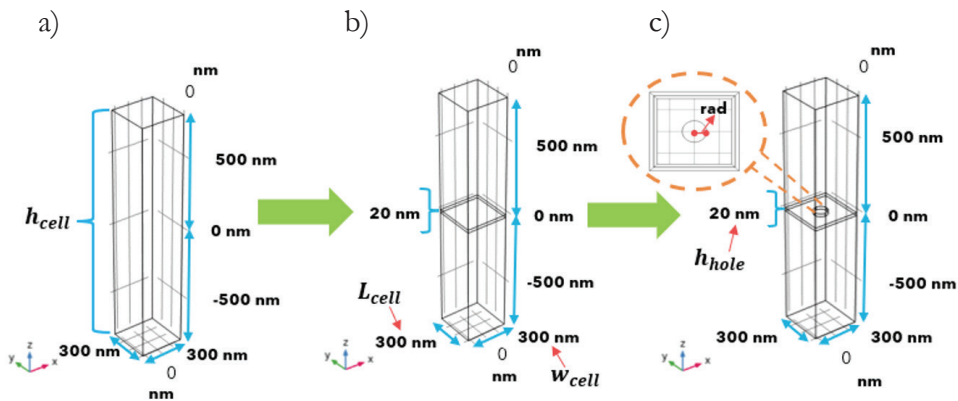


Figure 3. Steps and parameters for each section. (a). First step to start building the geometry and the parameters for the first block corresponding to the entire cell. (b) Second step, where the second block, the gold film, and its parameters are added. (c) Third step, where the cylinder and its measures are added to create the nanohole's geometry, notice that in this step the diameter varies from 90 to 130 nm.

### 2.3. Gold nanohole materials

The COMSOL Multiphysics material selection allowed to define the electromagnetic properties of the materials present in the model. By selecting and setting these properties for the dielectric medium, it was possible to model optical properties, such as transmittance, reflectance, and absorbance of

electromagnetic waves in different types of materials. To observe the behavior of the electric field as it passed through the gold cell and propagates through a dielectric medium, materials for each domain in the geometry had to be selected. First, air was chosen for the top domain of the geometry and the cylinder domain (Figure 4a). Air has a refractive index of  $n = 1$  and is already established by the software.

The second material selected for the simulation was gold, a noble metal that exhibits unique electronic and plasmonic properties including LSPR. Gold is biocompatible, making it suitable for biological applications. Gold was assigned to the second domain representing the thin gold film between the dielectric medium (air) and the glass substrate (see Figure 4b). The material Johnson and Christy 1972:  $n.k$  0.188-1.937  $\mu\text{m}$  was chosen because its refractive index is predefined by COMSOL. The plasmonic resonance of gold nanoparticles is influenced by their size, shape, and surrounding environment, therefore control over these characteristics determines the optical properties of gold nanoholes. Changes in the refractive index of the surrounding medium can significantly impact the optical properties of gold nanoholes. Finally, the bottom layer in the geometry (as shown in Figure 4c) represents the glass substrate, which can be composed of either Corning® Eagle XG® Glass or Corning® Gorilla® Glass Victus®. These materials are pre-defined in COMSOL with a refractive index of  $n = 1.5$ . Table 3 shows the materials with their refractive indices.

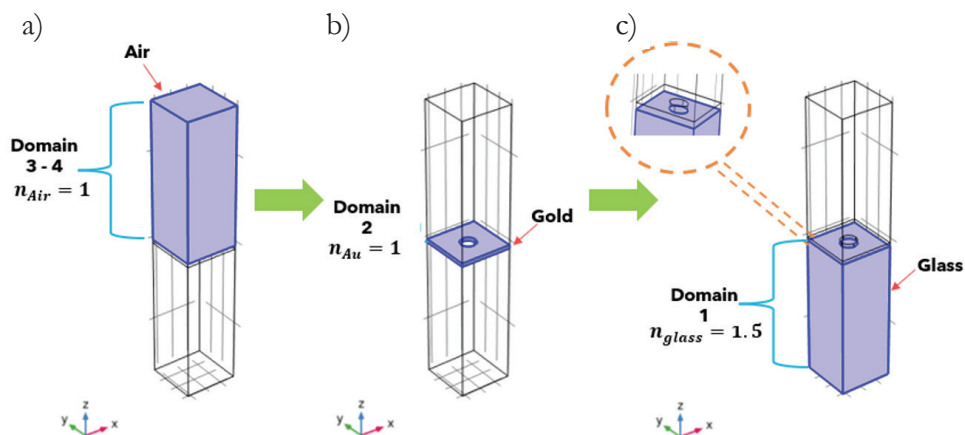


Figure 4. Structure's geometry sections. (a) The upper section (highlighted in blue) constitutes domains 3 and 4; this section represents air in the model with refractive index of  $n = 1$ .

(b) Domain 2 represents the gold nanofilm in the model with a refractive index defined by COMSOL. (c) The bottom section of the geometry, designated as Domain 1, is made of glass with refractive index of  $n = 1.5$ .

Material	Type	Extra settings
Air	Built in → Air	Refractive Index: Real part: 1 Imaginary part: 0
Gold	Au (Gold) (Johnson and Christy 1972: n,k 0.188-1.937 μm).	Refractive Index: Real part: n Imaginary part: k Predefined in COMSOL
Glass	Corning® Eagle XG® Glass. Or Corning® Gorilla® Glass Victus®.	Refractive Index: Real part: 1.5 Imaginary part: 0

Table 3. Material specifications of gold nanohole dielectric media.

## 2.4. Physics configuration

For this work, the Electromagnetic Waves, Frequency Domain (*enfd*) physics interface was used in COMSOL Multiphysics to model and simulate the behavior of an electromagnetic field across a range of wavelengths interacting with the gold nanohole. This section includes defining boundary conditions, setting up the source properties and establishing the mesh definition.

### 2.4.1. Ports

To start the physics configuration, Ports were set up to define the regions where the electromagnetic field enters and exits the model domain, as well as indicate the direction and amplitude of the electromagnetic field. In this model, the bottom face of the block labeled as Boundary 3 in COMSOL, was designated as the entry point (Figure 5a), thereby wave excitation was activated here, as specified in Table 4. The top face, labeled boundary 10 in COMSOL, was designated as the exit point for the transmitted light (Figure 5b) and the wave excitation option is turned off. The objective of this set up was to compute the amount of light absorbed, reflected, and transmitted through the nanohole at certain wavelengths.

Port	Type	Wave excitation	Input Quantity	Electric mode field amplitude	Refractive index, real part
Port 1	Periodic	On	Electric field	$x \rightarrow 1$ $y \rightarrow 0$ $z \rightarrow 0$	1.5
Port 2	Periodic	Off	Electric field	$x \rightarrow 1$ $y \rightarrow 0$ $z \rightarrow 0$	1

Table 4. Port properties set up.

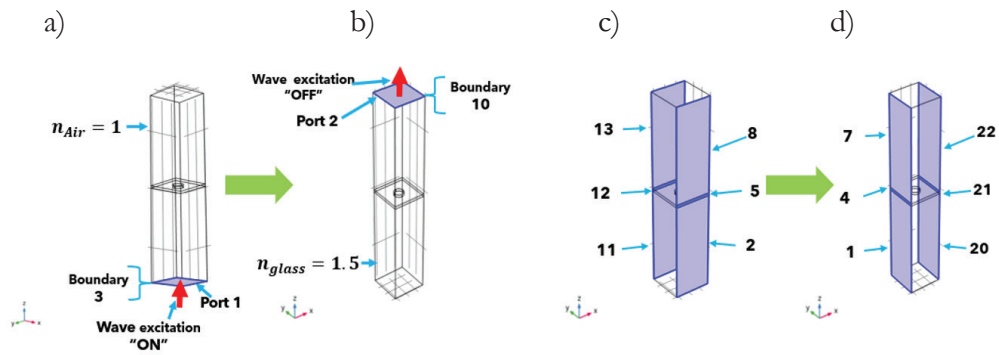


Figure 5. Physics configuration for the model. (a) Configuration of Port 1 (Boundary 3, bottom face), which serves as the Light source entry point. (b) Configuration for Port 3 (top face, boundary 10). (c) Boundary selection for periodic conditions 1. (d) Boundary selection for periodic conditions 2.

#### 2.4.2. Periodic Conditions

Periodic conditions were applied to confine the flow of the electromagnetic field within the model geometry and prevent energy leakage. In this simulation, which features a 4-sided block geometry, periodic boundary conditions are applied to two pairs of parallel sides, the selection process is illustrated in Figure 5c-d, which highlights the necessary parallel selection for the simulation. To avoid leakage during the simulation, all regions from each side must be selected.

#### 2.5. Mesh

The mesh divides the computational domain into smaller elements, allowing for the discretization of equations governing the model, for this study COMSOL Multiphysics uses FEM equations to solve for the electromagnetic fields within the gold nanohole and its surrounding medium.

In this simulation, the mesh is automatically generated by COMSOL Multiphysics, breaking down the domain into manageable units and maintain computational efficiency. The mesh coverage is shown in Figure 6a.

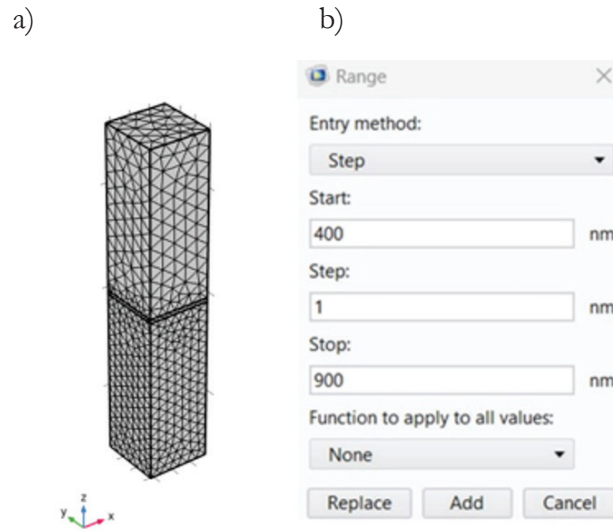


Figure 6. Mesh and wavelength. (a) Mesh selected determines the number of points examined, and the time the software will take to perform the calculations, thereby with a fine mesh, the computing time will take longer. (b) Wavelength range of interest for studying the optical properties of the gold nanohole. Note: The Step can be increased to minimize the time of computing, but the information will not be the same and the statistical values may be slightly different from each other.

## 2.6. Study configuration

The Study section in COMSOL is where the studies to be performed on the model were defined and configured, allowing to determine what type of analysis were carried out. In this simulation, the study section allowed the analysis of plasmonic gold nanohole behavior as a function of frequency to obtain optical properties (transmittance, reflectance, absorption), electromagnetic fields, and COMSOL solves the point-to-point mesh equations.

After setting up the physical characteristics of the system and establishing the geometry, the next step was to analyze the behavior of the electric field through the gold nanohole. This study was done by varying the wavelength of the electric field across a range from 400 nm to 900 nm in increments of 1 nm (Figure 6b). This wavelength range has been specifically selected because it corresponds to the excitation of the plasmon. The main objective of this study is to generate a

light transmittance spectrum across the entire cell, which provides information about the wavelengths that most excite the plasmon in the simulation.

## 2.7. Data extraction and export

The Results section in COMSOL provided an important tool for analyzing and understanding of the simulations performed by visualizing the data, generating graphs, and extracting important information about the behavior of the simulated system, including the electric field and optical properties. Once the simulation was completed, the behavior of each cell, as the plasmonic nanohole diameter was varied, can be easily analyzed by examining the optical properties and electric field. To visualize the electric field in COMSOL (Figure 7a), the “Volume” option in the Electric Field section was selected and the expression “ewfd.Ex” was entered, since it propagates in the x-direction through the cell. The Plot button on the Electric Field (ewfd) toolbar was selected to generate the appropriate visualization. Figure 7c shows graphs of transmission, reflection, and absorption properties. These properties are displayed in Reflectance, Transmittance, and Absorbance (ewfd) 1. To obtain each property, the above plot was duplicated, and the property of interest was selected in the Y-Axis Data Configuration window. The options for exporting the data obtained are shown in Figure 7b.

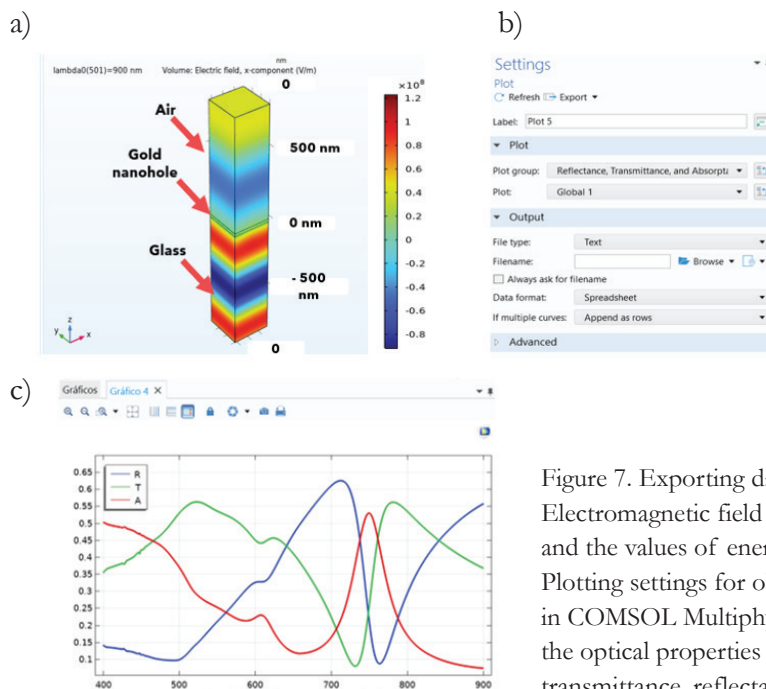


Figure 7. Exporting data. (a) Electromagnetic field of the gold nanohole and the values of energy at the scale. (b) Plotting settings for obtaining graph results in COMSOL Multiphysics. (c) Graphs of the optical properties of interest, such as transmittance, reflectance, and absorbance.

### 3. Results and Discussion

This section entails a numerical analysis comprising five simulations of a gold nanohole, each with varying diameters: 90 nm, 100 nm, 110 nm, 120 nm, and 130 nm. Within each simulation, the optical properties alongside the electric field in the x-direction for the nanohole to analyze the behavior of the cell when increasing the diameter of the nanohole were examined.

#### 3.1. Optical properties: 90 nm diameter nanohole

The initial diameter under examination is 90 nm for the nanohole. Figure 8 illustrates three optical properties representing the behavior of light through the cell, using the parameters established in the preceding section. These properties are correlated, and the simulation's accuracy can be confirmed by scrutinizing a specific wavelength on the graph. Summing all properties at their intersecting points along a vertical line in a point of interest should yield 1.0. In Figure 8, the arbitrary unit (a.u.) for each property is evident. For example, the transmittance value at 675 nm that wavelength measures 0.13985 a. u., reflectance stands at 0.4197 a. u., and absorbance records at 0.44045 a. u. When these properties are combined, they sum to 1.0 a. u., affirming that all incident light interacts with the cell and that there is no light leakage in the cell's configuration. The 675 nm wavelength value was selected because it represents the lowest point in transmittance, where the LSPR is manifested. However, any wavelength can be chosen, since the sum of all properties is equal 1 a. u.

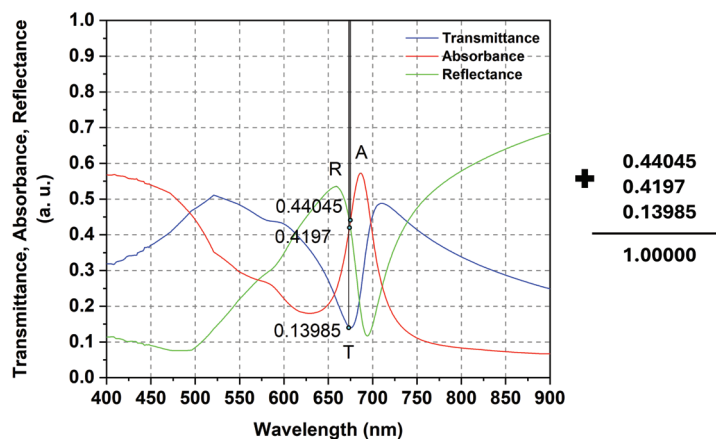


Figure 8. Correlation between the optical properties at one specific wavelength and its sum which equals 1 a.u. to prove the settings simulation by having all the energy interaction in the geometry.

Each property provides information about different behavior in geometry, each of them is useful for different applications. The transmittance (Figure 9a) gives information of the amount of light that arrives to the detector (output) for every wavelength in a range of 400 nm to 900 nm, this interaction is represented by the blue curve, the point of interest in this curve is the lowest point in the graph seeing that it is the value where the light is interacting all over the cell and a plasmon dipole is created by having oscillations with gold electrons and interactions with each other. This phenomenon can only be created with very stable noble metals like gold, due to its plasmonic properties. It is important to note that every design alters the LSPR wavelength. Changes in characteristics such as size, composition, and geometry in the simulation could provoke different LSPR responses. In this case, the plasmon dipole is created at the wavelength of 675 nm and generates an electric field in  $x$  direction with a value of  $8.033 \times 10^8$  V/m (see Table 6 for the maximum values of energy at each point of interest) [30, 31]. This can be observed in Figure 9b-c. The Figure 9b is the top view of the nanohole and the dipole can be seen on the gold film, while in the side view, Figure 9c, it is seen the interaction of the light all over the geometry and it is observed how the dipole is created only in the surface of the nanohole by having gold electron oscillations. With the sidebar color, it is evident that interactions primarily occur within the noble metal, resulting in the highest electric field value (red color) concentrated around the nanohole.

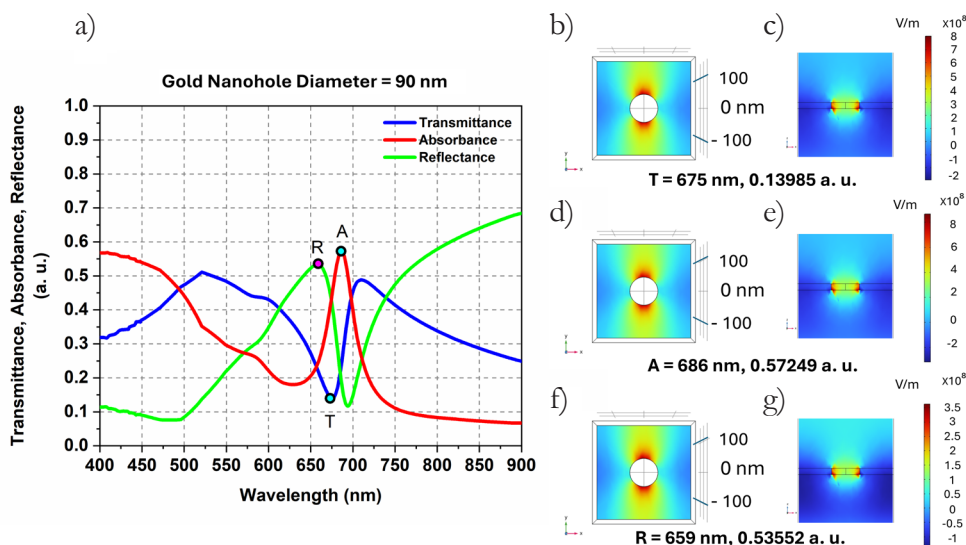


Figure 9. (a) Transmittance, absorbance, and reflectance curves for the 90 nm diameter gold nanohole and its wavelengths at which the plasmon originates for each property. (b), (d), (f) Top view of the gold film at those points of interest for transmittance, absorbance, and reflectance, and (c), (e), (g) side view of plasmon interaction with air (top), gold (center), and glass (bottom) at those same points.

The absorbance (Figure 9d-e) gives information of the amount of light that is absorbed by the gold. In this case, the red curve exhibits the light interaction over the cell for every wavelength with a range of 400 nm to 900 nm where the point of interest is the highest point where the energy is interacting with the nanohole in a wavelength of 686 nm and creating an Ex of  $8.65 \times 10^8$  V/m.

For the reflectance (Figure 9f-g), this property gives information of the amount of light that returns to the light source when it is interacting over the cell, this interaction is represented by the green curve and the point of interest is the highest point of the curve because it is the greatest amount of light that returns to the light source at the wavelength of 659 nm. At this wavelength the plasmon interaction has an Ex of  $3.63 \times 10^8$  V/m, in this value the plasmon dipole is generated. Thus, it was shown that LSPR is present at the point of interest of each property.

### **3.2. *Optical properties: 100 nm diameter nanohole***

For the 100 nm nanohole and the subsequent ones (110 nm, 120 nm, and 130 nm) the image distribution is the same as indicated for the 90 nm nanohole. Figure 10a shows a graph with three different curves with the following colors: blue for transmittance (T), red for absorbance (A) and green for reflectance (R). In every curve there is a highlighted point for T, A, R, respectively, that indicates where the plasmon dipole is created. Then, Figure 10b, Figure 10d, and Figure 10f show the top view of the nanohole at that specific wavelength and Figure 10c, Figure 10e, and Figure 10g the side view of the entire geometry and how the light interacts with the different cell materials (air at the top, gold at the center and glass at the bottom).

In this case, for the T point, the minimum value of the curve indicates that the plasmon originates at a wavelength of 684 nm and has a maximum energy value of  $9.28 \times 10^8$  V/m. The A point, the maximum value of the curve, originates at a wavelength of 697 nm and has a maximum energy value of  $6.48 \times 10^8$  V/m, and finally the R point, the maximum of the curve, originates at a wavelength of 663 nm and has a maximum energy value of  $4.03 \times 10^8$  V/m. Notice that the wavelength at which the plasmon originates, has shifted to the right compared to the 90 nm diameter nanohole: 9 nm for T, 11 nm for A, and 4 nm for R. Since the accuracy of the simulation was established, the verification process with the vertical line in the three optical properties for this diameter or subsequent one was done. This step was previously demonstrated and confirmed in Figure 8, affirming the validity of the results obtained.

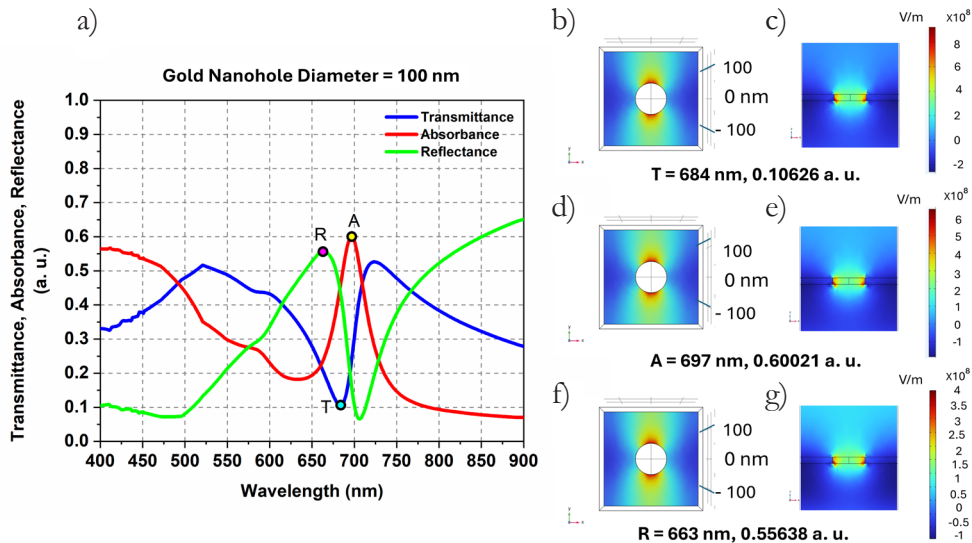


Figure 10. (a) Transmittance, absorbance, and reflectance curves for the 100 nm diameter gold nanohole and its wavelengths at which the plasmon originates for each property. (b), (d), (f) Top view of the gold film at those points of interest for transmittance, absorbance, and reflectance, and (c), (e), (g) side view of plasmon interaction with air (top), gold (center), and glass (bottom) at those same points.

### 3.3. *Optical properties: 110 nm diameter nanohole*

With the 110 nm diameter nanohole (Figure 11) for the T point the plasmon originates at a wavelength of 685 nm, has a maximum energy value of  $7.8 \times 10^8$  V/m. For the A point originates at a wavelength of 700 nm and has a maximum energy value of  $6.65 \times 10^8$  V/m, and for the R point originates at a wavelength of 666 nm and has a maximum energy value of  $3.81 \times 10^8$  V/m. Focus on the displacement of the wavelength where the plasmon originates, which has been shifted to the right compared to the 100 nm diameter nanohole: 1 nm for T, 3 nm for A, and 3 nm for R. However, this time the shifts have not been as significant as with the previous one.

In this scenario, we note a decrease in the values of the electric field for transmittance (T), which contrasts with the observed increase from a diameter of 90 nm to 100 nm. This observation prompts a more detailed analysis of the electric field values for subsequent diameters to pinpoint where the highest electric field energy is concentrated. Such insight can guide in identifying the most optimal diameters for transducer nanofabrication.

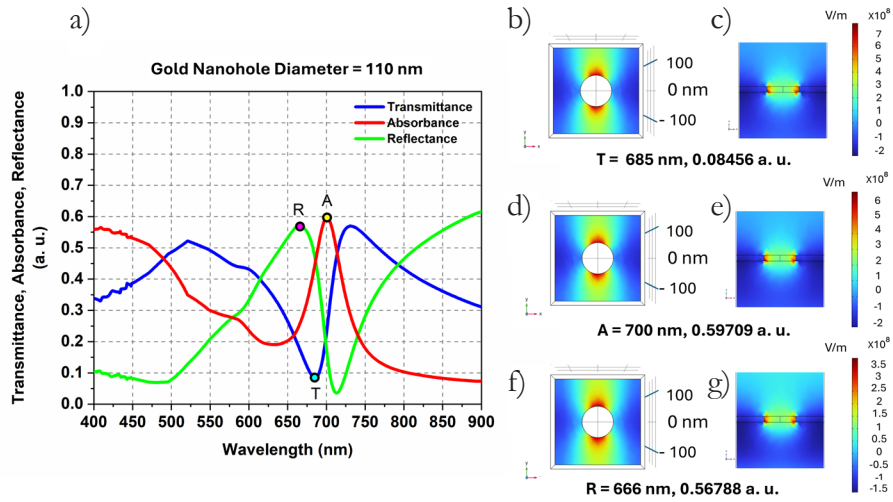


Figure 11. (a) Transmittance, absorbance, and reflectance curves for the 110 nm diameter gold nanohole and its wavelengths at which the plasmon originates for each property. (b), (d), (f) Top view of the gold film at those points of interest for transmittance, absorbance, and reflectance, and (c), (e), (g) side view of plasmon interaction with air (top), gold (center), and glass (bottom) at those same points.

### 3.4. Optical properties: 120 nm diameter nanohole

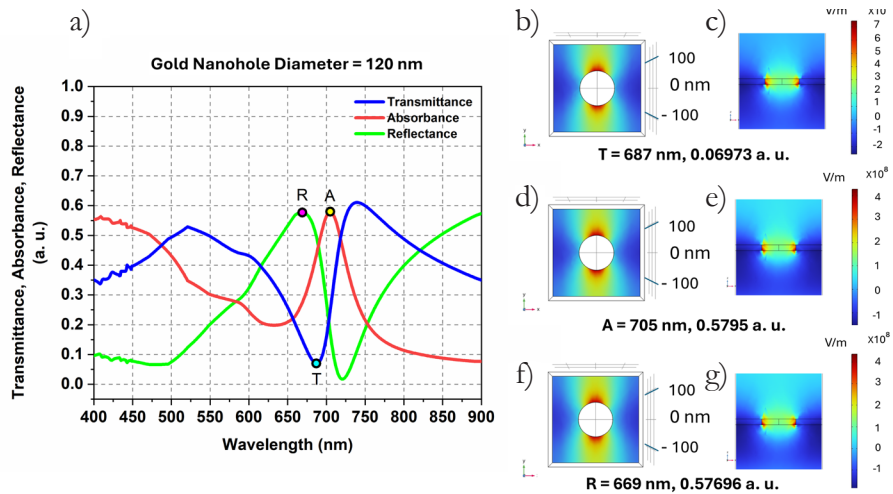


Figure 12. (a) Transmittance, absorbance, and reflectance curves for the 120 nm diameter gold nanohole and its wavelengths at which the plasmon originates for each property. (b), (d), (f) Top view of the gold film at those points of interest for transmittance, absorbance, and reflectance, and (c), (e), (g) side view of plasmon interaction with air (top), gold (center), and glass (bottom) at those same points.

Subsequently, we increment the diameter by 10 units to 120 nm (Figure 12) and observe the peak energy values: for the T point, originating at a wavelength of 687 nm, the electric field strength reaches  $7.42 \times 10^8$  V/m; for the A point, originating at a wavelength of 705 nm, it measures  $4.28 \times 10^8$  V/m, and for the R point, originating at a wavelength of 669 nm, it registers at  $4.36 \times 10^8$  V/m. Notably, the wavelength of plasmon excitation shifts further rightward: by 2 units for T, 5 units for A, and 2 units for R. Remarkably, energy levels decrease at every point except for point R, where an increase is observed.

### 3.5. Optical properties: 130 nm diameter nanohole

Finally, for the 130 nm diameter hole (Figure 13), we get the maximum energy values: for the T point at a wavelength of 690, with  $5.88 \times 10^8$  V/m; for the A point originated at a wavelength of 710 nm, with  $3.52 \times 10^8$  V/m, and for the R point originated at a wavelength of 673 nm, with  $3.6 \times 10^8$  V/m. The wavelength at which the plasmon originated keeps on moving to the right: 3 units for T, 5 units for A, and 4 units for R. The energy has decreased at every point without exceptions.

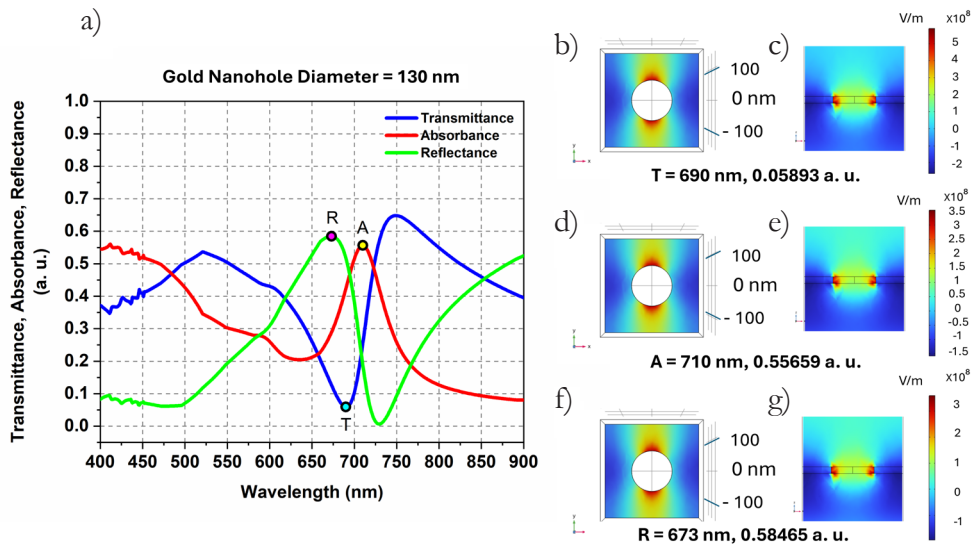


Figure 13. (a) Transmittance, absorbance, and reflectance curves for the 130 nm diameter gold nanohole and its wavelengths at which the plasmon originates for each property. (b), (d), (f) Top view of the gold film at those points of interest for transmittance, absorbance, and reflectance, and (c), (e), (g) side view of plasmon interaction with air (top), gold (center), and glass (bottom) at those same points.

The optical properties analysis reveals a notable wavelength displacement as the nanohole diameter increases. This displacement is observed in the transmittance (Figure 14a-b), absorbance (Figure 14c-d), and reflectance spectra (Figure 14e-f). Notably, altering the cell geometry by enlarging the diameter while reducing the gold area induces a rightward shift in the curves.

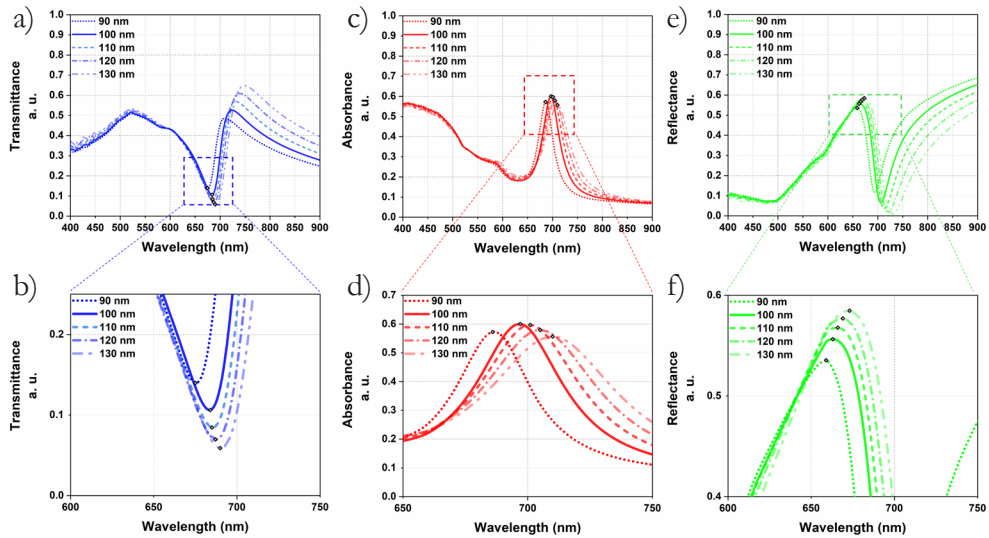


Figure 14. (a) Transmittance, (b) Absorbance and (c) Reflectance graphs for different gold nanohole diameters: 90 nm, 100 nm, 110 nm, 120 nm, and 130 nm.

For instance, with a 90 nm diameter, the transmittance curve initiates at a wavelength of 675 nm and terminates at 690 nm for the 130 nm diameter, resulting in a 15 nm rightward displacement. Similarly, the absorbance curve commences at 686 nm for the 90 nm diameter and extends to 710 nm for the 130 nm diameter, producing a 24 nm shift to the right. Reflectance, beginning at 659 nm and concluding at 673 nm, generates a 14 nm displacement. These findings highlight the influence of geometry alterations on optical properties, primarily attributed to increased diameter and reduced gold area. Notably, despite these changes, each proposed diameter retains the ability to induce Localized Surface Plasmon Resonance (LSPR), as evidenced by the consistent shape of the optical property curves across different geometries, with only the displacement varying (Figure 14). Detailed values of these curves are presented in Table 5.

Nanohole Diameter	LSPR Wavelength (nm) / Minimum in Transmittance (a. u.)	LSPR Wavelength (nm) / Maximum in Absorbance (a. u.)	LSPR Wavelength (nm) / Maximum in Reflectance (a. u.)	Gold Area (%)
90	675, 0.13985	686, 0.57249	659, 0.53552	92.93
100	684, 0.10626	697, 0.60021	663, 0.55638	91.27
110	685, 0.08456	700, 0.59709	666, 0.56788	89.44
120	687, 0.06973	705, 0.5795	669, 0.57696	87.43
130	690, 0.05893	710, 0.55659	673, 0.58465	85.25

Table 5. Comparison between the different diameters and its arbitrary units (a.u.) maximum, for absorbance and reflectance, and minimum values, for transmittance, at which the plasmon dipole (LSPR) originates, and the percentage of gold area obtained with every diameter, that match the literature. [30, 32].

Furthermore, the analysis of the electric field at the focal point of interest, particularly in relation to transmittance, offers significant insights into the light's behavior within the geometry. It elucidates how oscillations in gold electrons generate a dipole effect. Note that the intensity of the electric field (see Table 6) is notably higher in the first two diameters, namely 90 nm and 100 nm, with the highest value recorded at 100 nm, reaching  $9.98 \times 10^8$  V/m.

Based on these numerical findings, it is recommended that for the nanofabrication of optical transducers relying on nanoholes, a diameter of 100 nm should be chosen. This diameter presents several advantages, including the availability of various vendors guaranteeing its specific size, thus simplifying the nanofabrication process. Conversely, opting for other diameters would necessitate meticulous nanofabrication techniques to ensure precise diameter consistency across all holes.

Therefore, the recommendation stands to fabricate optical transducers with a 100 nm diameter to achieve optimal performance within the geometry and streamline the nanofabrication process.

Nanohole Diameter	Optical property	Electric field maximum value (V/m)	LSPR Wavelength (nm)
90 nm	Transmittance	$8.03 \times 10^8$	675
	Absorbance	$8.65 \times 10^8$	686
	Reflectance	$3.63 \times 10^8$	659
100 nm	Transmittance	$9.28 \times 10^8$	684
	Absorbance	$6.48 \times 10^8$	697
	Reflectance	$4.03 \times 10^8$	663
110 nm	Transmittance	$7.80 \times 10^8$	685
	Absorbance	$6.65 \times 10^8$	700
	Reflectance	$3.81 \times 10^8$	666
120 nm	Transmittance	$7.42 \times 10^8$	687
	Absorbance	$4.28 \times 10^8$	705
	Reflectance	$4.36 \times 10^8$	669
130 nm	Transmittance	$5.88 \times 10^8$	690
	Absorbance	$3.52 \times 10^8$	710
	Reflectance	$3.60 \times 10^8$	673

Table 6. Electric field maximum energy values for each diameter nanohole at its different properties at the wavelength where the plasmon originated, that match the literature. [20, 21].

#### 4. Conclusions

In this work, a numerical analysis of the diameter of a nanoplasmonic transducer based on gold nanoholes is presented. Thereby, a study of the gold percentage to induce plasmonic resonances is analyzed.

Simulations explored nanohole diameters ranging from 90 nm to 130 nm, revealing significant effects on optical properties. As the diameter increased, the wavelength of Localized Surface Plasmon Resonance (LSPR) for transmittance (T, 675 nm), absorbance (A, 686 nm), and reflectance (R, 659 nm) shifted 15 nm, 24 nm and 14 nm towards longer wavelengths, respectively. Despite a reduction in the percentage of gold area ( $900 \text{ nm}^2$ ) from 92.93 % to 85.25 %, the curves for transmittance, absorbance, and reflectance continued to exhibit

the LSPR phenomenon. The optical curves showed slight changes in the width and depth. The transmittance (T) changed from 0.139 a. u. to 0.058 a. u., the absorbance (A) from 0.572 a. u. to 0.556 a. u. and reflectance (R) from 0.535 a. u. to 0.584 a. u. Additionally, the electric field distributions of the plasmon dipole indicated that a gold nanohole with a diameter of 100 nm had the highest intensity of  $9.28 \times 10^8$  V/m, suggesting this configuration for optical transducer fabrication. Despite variations in nanohole diameter, all configurations maintain the ability to induce LSPR within the visible spectrum. This recommendation is supported by practical benefits like easier access from various suppliers and simpler fabrication processes. Therefore, this study emphasizes the importance of diameter selection to optimize the performance of optical transducers, which could enhance sensitivity, selectivity, and detection limits. By considering these insights, researchers and new students can improve the functionality and effectiveness of plasmonic transducers, particularly in bioanalytical applications.

### **Acknowledgement**

The authors would like to thank the Instituto Politécnico Nacional for the use of its facilities, as well as the BEIFI SIP20240477, SIP20241266, and PRORED 20243969 projects. Additionally, we extend our gratitude to CONAHCYT for its support through postgraduate scholarships and for the project CONAHCYT N°319037 “Escuela Mexicana de Ventilación”.

## References

1. Lu, X., Rycenga, M., Skrabalak, S. E., Wiley, B., & Xia, Y. (2009). Chemical Synthesis of Novel Plasmonic Nanoparticles. *Annual Review of Physical Chemistry*, *60*(1), 167–192. <https://doi.org/10.1146/annurev.physchem.040808.090434>
2. Ebbesen, T. W., Lezec, H. J., Ghaemi, H. F., Thio, T., & Wolff, P. A. (1998). Extraordinary optical transmission through sub-wavelength hole arrays. *Nature*, *391*(6668), 667–669. <https://doi.org/10.1038/35570>
3. Cottat, M., Goyard, D., Manesse, M., Varenne, C., & Chassagneux, Y. (2013). Localized Surface Plasmon Resonance (LSPR) Biosensor for the Protein Detection. *Plasmonics*, *8*(2), 699–704. <https://doi.org/10.1007/s11468-012-9460-3>
4. Samsuri, N. D., Mukhtar, W. M., Rashid, A. R. A., Dasuki, K. A., & Yussuf, A. A. R. H. A. (2017). Synthesis methods of gold nanoparticles for Localized Surface Plasmon Resonance (LSPR) sensor applications. *EPJ Web of Conferences*, *162*, 01002. <https://doi.org/10.1051/epjconf/201716201002>
5. Dos Santos, P. S. S., Gomes, A. L., Peres, D. R. M., Fonseca, D. R., Rodrigues, D. A., De Freitas, D. S., ... & Zucolotto, V. (2023). Spectral Analysis Methods for Improved Resolution and Sensitivity: Enhancing SPR and LSPR Optical Fiber Sensing. *Sensors*, *23*(3), 1666. <https://doi.org/10.3390/s23031666>
6. Kastner, S., Mayr, K., Ziegler, S., & Sinner, E.-K. (2023). LSPR-Based Biosensing Enables the Detection of Antimicrobial Resistance Genes. *Small*, *19*(33), 2207953. <https://doi.org/10.1002/sml.202207953>
7. Mayer, K. M., & Hafner, J. H. (2011). Localized surface plasmon resonance sensors. *Chemical Reviews*, *111*(6), 3826–3857. <https://doi.org/10.1021/cr100313v>
8. Solis-Tinoco, V., Marquez, S., Quesada-Lopez, T., Villarroya, F., Homs-Corbera, A., & Lechuga, L. M. (2019). Building of a flexible microfluidic plasmo-nanomechanical biosensor for live cell analysis. *Sensors and Actuators B: Chemical*, *291*, 48–57. <https://doi.org/10.1016/j.snb.2019.04.038>
9. Jazayeri, M. H., Aghaie, T., Nedaeinia, R., Manian, M., & Nickho, H. (2020). Rapid noninvasive detection of bladder cancer using survivin antibody-conjugated gold nanoparticles (GNPs) based on localized surface plasmon resonance (LSPR). *Cancer Immunology, Immunotherapy*, *69*(9), 1833–1840. <https://doi.org/10.1007/s00262-020-02559-y>

10. Lertvachirapaiboon, C., Baba, A., Shinbo, K., & Kato, K. (2021). Colorimetric detection based on localized surface plasmon resonance for determination of chemicals in urine. *Analytical Sciences*, 37(7).  
<https://doi.org/10.2116/analsci.20R005>
11. António, M., Vitorino, R., & Daniel-da-Silva, A. L. (2023). LSPR-based aptasensor for rapid urinary detection of NT-proBNP. *Biosensors*, 13(7).  
<https://doi.org/10.3390/bios13070736>
12. Biosensors. (2024). Recent advancements of LSPR fiber-optic biosensing: Combination methods, structure, and prospects. *MDPI*. Retrieved April 10, 2024, from:  
<https://www.mdpi.com/2079-6374/13/3/405>
13. Paul, D., & Biswas, R. (2022). Clad modified varying geometries of fiber optic LSPR sensors towards detection of hazardous volatile liquids and their comparative analysis. *Environmental Technology & Innovation*, 25, 102112.  
<https://doi.org/10.1016/j.eti.2021.102112>
14. Wei, X. Z., & Mulvaney, P. (2014). Optical properties of strongly coupled plasmonic nanoparticle clusters. In N. V. Richardson & S. Holloway (Eds.), *Handbook of Surface Science, Modern Plasmonics* (Vol. 4, pp. 75–108). North-Holland.  
<https://doi.org/10.1016/B978-0-444-59526-3.00003-3>
15. IntechOpen. (2024). The influence of geometry on plasmonic resonances in surface- and tip-enhanced Raman spectroscopy. Retrieved April 10, 2024, from:  
<https://www.intechopen.com/chapters/84716>  
<https://doi.org/10.5772/intechopen.108182>
16. Wang, H., et al. (2023). Plasmonic nanostructure biosensors: A review. *Sensors*, 23(19).  
<https://doi.org/10.3390/s23198156>
17. Kim, D. M., Park, J. S., Jung, S.-W., Yeom, J., & Yoo, S. M. (2021). Biosensing applications using nanostructure-based localized surface plasmon resonance sensors. *Sensors*, 21(9).  
<https://doi.org/10.3390/s21093191>
18. De Leebeeck, A., Kumar, L. K. S., de Lange, V., Sinton, D., Gordon, R., & Brolo, A. G. (2007). On-chip surface-based detection with nanohole arrays. *Analytical Chemistry*, 79(11), 4094–4100.  
<https://doi.org/10.1021/ac070001a>
19. Gomez-Cruz, J., Nair, S., Ascanio, G., & Escobedo, C. (2017). Flow-through nanohole array-based sensor implemented on analogue smartphone components. In *Proceedings of SPIE* (Vol. 10395, p. 80).  
<https://doi.org/10.1117/12.2272433>

20. Hosseinpour, M., Zendehnam, A., Hamidi Sangdehi, S. M., & Ghomi Marzdashti, H. (2021). Simulation of the improvement in the performance of a silver-based surface plasmon resonance biosensor using experimental results of cold plasma treatment of glass substrate. *Journal of Computational Science*, *54*, 101410.  
<https://doi.org/10.1016/j.jocs.2021.101410>
21. Zhao, E., et al. (2017). Localized surface plasmon resonance sensing structure based on gold nanohole array on beveled fiber edge. *Nanotechnology*, *28*(43), 435504.  
<https://doi.org/10.1088/1361-6528/aa847a>
22. Li, X., Soler, M., Özdemir, C. I., Belushkin, A., Yesilköy, F., & Altug, H. (2017). Plasmonic nanohole array biosensor for label-free and real-time analysis of live cell secretion. *Lab on a Chip*, *17*(13), 2208–2217.  
<https://doi.org/10.1039/C7LC00277G>
23. Escobedo, C. (2013). On-chip nanohole array-based sensing: A review. *Lab on a Chip*, *13*(13), 2445–2463.  
<https://doi.org/10.1039/C3LC50107H>
24. Ferreira, J., et al. (2009). Attomolar protein detection using in-hole surface plasmon resonance. *Journal of the American Chemical Society*, *131*(2), 436–437.  
<https://doi.org/10.1021/ja807704v>
25. Gomez-Cruz, J., Nair, S., Manjarrez-Hernandez, A., Gavilanes-Parra, S., Ascanio, G., & Escobedo, C. (2018). Cost-effective flow-through nanohole array-based biosensing platform for the label-free detection of uropathogenic *E. coli* in real time. *Biosensors and Bioelectronics*, *106*, 105–110.  
<https://doi.org/10.1016/j.bios.2018.01.055>
26. Wang, Y., Chong, H. B., Zhang, Z., & Zhao, Y. (2020). Large-area fabrication of complex nanohole arrays with highly tunable plasmonic properties. *ACS Applied Materials & Interfaces*, *12*(33), 37435–37443.  
<https://doi.org/10.1021/acscami.0c06936>
27. Jia, H., Fredriksson, H., Hole-Mask, C. L., et al. (2022). Plasmonic nanohole arrays with enhanced visible light photoelectrocatalytic activity. *ACS Photonics*, *9*(2), 652–663.  
<https://doi.org/10.1021/acsp Photonics.1c01684>
28. Fredriksson, H., Alaverdyan, Y., Dmitriev, A., Höök, F., Langhammer, C., Sutherland, D. S., Zäch, M., & Käll, M. (2007). Hole–mask colloidal lithography. *Advanced Materials*, *19*(23), 4297–4302.  
<https://doi.org/10.1002/adma.200700680>
29. Wang, Q., & Wang, L. (2020). Lab-on-fiber: Plasmonic nano-arrays for sensing. *Nanoscale*, *12*(14), 7485–7499.  
<https://doi.org/10.1039/D0NR00040J>

30. Colombelli, A., Manera, M. G., Rella, R., & Vasanelli, L. (2014). FEM modeling of nanostructures for sensor application. In C. Di Natale, V. Ferrari, A. Ponzoni, G. Sberveglieri, & M. Ferrari (Eds.), *Sensors and Microsystems* (pp. 287–291). Springer International Publishing.  
[https://doi.org/10.1007/978-3-319-00684-0\\_55](https://doi.org/10.1007/978-3-319-00684-0_55)
31. Hsiao, A., Gartia, M. R., Chang, T.-W., Wang, X., Khumwan, P., & Liu, G. L. (2015). Colorimetric plasmon resonance microfluidics on nanohole array sensors. *Sensors and Bio-Sensors Research*, 5, 24–32.  
<https://doi.org/10.1016/j.sbsr.2015.06.001>
32. Agharazy Dormeny, A., Abedini Sohi, P., & Kahrizi, M. (2020). Design and simulation of a refractive index sensor based on SPR and LSPR using gold nanostructures. *Results in Physics*, 16, 102869.  
<https://doi.org/10.1016/j.rinp.2019.102869>